



# Polarimetric Radar Signatures in Various Lightning Activities During Seoul (Korea) Flood on August 8, 2022

Hee-Ae Kim<sup>1</sup> · Junho Ho<sup>2,3</sup> · Guifu Zhang<sup>2,3</sup> · Kyung-Ja Ha<sup>4</sup> · Song-You Hong<sup>5</sup> · Chang-Hoi Ho<sup>1,6</sup>

Received: 3 August 2023 / Revised: 21 October 2023 / Accepted: 9 November 2023  
© The Author(s) 2023

## Abstract

On August 8 and 9, 2022, a record-breaking rain rate of 142 mm h<sup>-1</sup>, with an accumulated rainfall of more than 500 mm, was observed in the Seoul metropolitan area, Republic of Korea. This study focuses on analyzing the concentration of lightning in southern Seoul, which occurred solely on August 8. It is worth noting that the daily rainfall of August 8 was approximately twice that of August 9 (381 mm on August 8 vs. 198 mm on August 9). The RKSG (located in Yongin, 40 km south of Seoul) Weather Surveillance Radar-1988 Doppler was used to explore the characteristics of cloud microphysics associated with lightning activity. Four major heavy rain periods on August 8 were grouped into three categories of lightning rate (e.g., intense, moderate, and none), and their polarimetric signatures were compared. Significant differences in the vertical distribution of graupel were found within the temperature range of 0 °C and –20 °C, as indicated by radar reflectivity ( $Z_H$ ) > 40 dBZ and differential reflectivity ( $Z_{DR}$ ) < 0.5 dB. Although graupel was detected in all three categories at the relatively warm temperatures of 0 °C to –10 °C, its presence extended into colder regions exclusively in the intense category. This observation preceded the appearance of lightning by approximately 6 min. At heights with temperature ≤ –20 °C, a high concentration of vertically aligned ice crystals was observed in lightning-prone regions, leading to a decrease in differential phase ( $\Phi_{DP}$ ). In summary, this study provides valuable insights into the microphysical characteristics of thunderstorms and their relationship to lightning activity in the Seoul metropolitan area.

**Keywords** Seoul Flood · Lightning · Heavy Precipitation · Cloud Microphysics · Hydrometeor · Radar

## 1 Introduction

On August 8 and 9, 2022, the Seoul metropolitan area (SMA) in the Republic of Korea (hereafter referred to as Korea) experienced an onslaught of rainfall, exceeding

500 mm, along with a record-breaking heavy rain rate of 141.5 mm h<sup>-1</sup>. Roads and buildings throughout the SMA were flooded, resulting in sixteen fatalities and over \$51 million (US) in property damage (National Assembly Research Service, personal communication, 2022). The Korea Meteorological Administration (KMA) had issued warnings several days prior, predicting extreme rain rates of 60–100 mm h<sup>-1</sup> and lightning in the SMA. However, what was unexpected was that lightning was concentrated only between 12–22 local time (LT, 10-h period) on August 8, with no reports on August 9. The cumulative number of flashes during the 10 h was over 800, with the highest rate of over 300 h<sup>-1</sup> around 20 LT on August 8.

Presently, the KMA typically issues lightning forecasts when strong convective clouds are expected (Kar and Ha 2003; Hyun et al. 2010). The poor performance of the KMA's lightning forecasts is not a matter of public concern, as the damage caused by lightning is generally localized in space and time compared to other extreme weather events such as floods, landslides, and strong winds. Nevertheless,

✉ Chang-Hoi Ho  
hoch@ewha.ac.kr

<sup>1</sup> School of Earth and Environmental Sciences, Seoul National University, Seoul, Republic of Korea

<sup>2</sup> School of Meteorology, University of Oklahoma, Norman, OK, USA

<sup>3</sup> Advanced Radar Research Center, Norman, OK, USA

<sup>4</sup> Center for Climate Physics, Institute for Basic Science, Department of Atmospheric Sciences, Pusan National University, Busan, Republic of Korea

<sup>5</sup> Cooperative Institute for Research in Environmental Science, University of Colorado, Boulder, CO, USA

<sup>6</sup> Department of Climate and Energy Systems Engineering, Ewha Womans University, Seoul 03760, Republic of Korea

lightning should not be overlooked as it frequently causes equipment damage, electrical fires, and electric shock (e.g., Renni et al. 2010; Veraverbeke et al. 2017). In Korea, lightning results in an average of four fatalities per year (a KMA forecaster, personal communication, August 2019). Therefore, it is essential to recognize the serious consequences of lightning and take appropriate measures to mitigate its impact.

Lightning is a transient electric discharge, often occurring when rimmed ice particles (i.e., graupel) collide with ice crystals, and charges are separated by strong updrafts (Takahashi 1978; Price and Rind 1992; Saunders 2008). During the non-inductive collisions, the ice particles become charged regardless of a pre-existing electric field and result in electrical discharge (i.e., lightning) when the electric field increases sufficiently to cause insulating-air breakdown, making it conductive. The polarity of lightning was determined by the temperature and cloud liquid water contents of the environment (Takahashi 1978). Previous studies revealed that lightning flashes become more frequent under specific conditions, especially with strong updrafts ( $\geq 10 \text{ m s}^{-1}$ ) and increased graupel and/or hail mass at temperature heights between  $-10 \text{ }^\circ\text{C}$  and  $-40 \text{ }^\circ\text{C}$  (e.g., Schultz et al. 2015, 2017; Deierling et al. 2008, Deierling and Petersen 2008).

Understanding the occurrence of lightning provides insight into cloud development and the associated microphysical properties. Microphysical processes such as droplet condensation, collision, and evaporation are affected by the electric field inside the cloud (Nielsen et al. 2011). For instance, the position of the lightning activity was found to be linked to the storm precipitation structure and the distribution of areal precipitation amounts in the stratiform precipitation region in a mesoscale convective system (Rutledge and MacGorman 1988). Moreover, the lightning rate in the mixed layer of clouds was influenced by the life cycle of the storm (MacGorman et al. 2008). Lu et al. (2022) showed that the merging of convective cells leads to numerous particle collisions, which subsequently increases the mass of graupel and ice crystals in the clouds, ultimately triggering lightning jumps.

Cloud microphysical processes associated with lightning can be analyzed using dual-polarization radar observations, which provide information on the shape, size, orientation, and uniformity of hydrometeors (e.g., Takahashi et al. 2015; Mattos et al. 2016, 2017; Wang et al. 2022; Ho et al. 2023). The polarimetric radar variables, such as radar reflectivity factor at horizontal polarization ( $Z_H$ , hereafter referred to as reflectivity), differential reflectivity ( $Z_{DR}$ ), and correlation coefficients ( $\rho_{hv}$ ), exhibit notable variations depending on the presence of lightning within a storm and the stage of thunderstorm growth (Mattos et al. 2016, 2017; Wang et al.

2022). Takahashi et al. (2015) also used polarimetric radar to explain that clouds with lightning primarily form over land and are characterized by a mixed layer with graupel, whereas heavy rain clouds without lightning tend to originate over the ocean, resulting in a mixed layer with a high proportion of frozen droplets.

It is essential to understand lightning initiation in order to predict and prepare for potential damage from thunderstorms, as lightning is directly linked to storm development. Thus, we aim to examine the relationship between lightning activity and the variation of cloud hydrometeors in summer thunderstorms through the application of polarimetric radar observations. By analyzing polarimetric signatures, it is possible to infer the timing and the location of lightning occurrence. This finding could help to accurately forecast severe weather events and implement preventive measures. The remainder of this article is organized as follows: Sect. 2 outlines the data and methods used, Sect. 3 provides an overview of the Seoul flood episode, and Sect. 4 presents a comparative analysis of the radar data with lightning activity. Finally, Sect. 5 offers a conceptual illustration and in-depth discussions of the findings.

## 2 Data and Methods

### 2.1 Lightning Observation

Since 2015, the KMA has been operating lightning detection network (LINET) systems equipped with very low frequency (VLF)/low frequency (LF) sensors at twenty locations across the country. The LINET, established by the University of Munich, has been deployed in numerous countries worldwide, including most of Europe, Brazil, Australia, and Benin (Betz et al. 2009). The VLF/LF sensor estimates the location of lightning events by analyzing the waveform signal of the electromagnetic field that spreads out around the point of impact of the lightning (Betz et al. 2008). The sensor further calculates the time of occurrence, the geographical location in latitude and longitude, and the altitude of the lightning by measuring the time difference between signals detected at different observation points within the frequency range of 3–300 kHz (Betz et al. 2008). While this sensor has the capability to detect and discriminate between cloud-to-ground and intra-cloud lightning, this study utilized total lightning (hereafter referred to as lightning), a collective term encompassing both types. The sensor has a range of up to 250 km, with a position-detection accuracy of 100–250 m for cloud-to-ground lightning (Betz et al. 2004). For further technical details on error characteristics, data pre-processing, and filtering, refer to Betz et al. (2009).

## 2.2 Dual-polarization Radar Observation

The S-band dual-polarization RKSG Weather Surveillance Radar-1988 Doppler (WSR-88D, also known as NEXRAD) observations were obtained from the National Centers for Environmental Information ([www.ncei.noaa.gov](http://www.ncei.noaa.gov)). The radar performed volumetric scans at 5-min intervals, with a frequency of 2.94 GHz, a beam width of approximately  $0.925^\circ$ , and a range resolution of 250 m. While the KMA Weather Radar Center operates the S-band dual-pol radar network close to the research area, the radar (located on Mt. Gwanak in southern Seoul) was too close ( $< 10$  km) to the lightning flash location and was also damaged by extreme rainfall prior to the most active lightning period in this study. Similarly, the S-band radar at Mt. Yebong (located just outside of eastern Seoul), operated by the Ministry of Environment, was installed for hydrological purposes and collects only low elevation data at approximately 1-min intervals. Therefore, only RKSG radar observations were analyzed in the following. Polarimetric variables, including  $Z_H$ ,  $Z_{DR}$ ,  $\rho_{hv}$ , and differential phase ( $\Phi_{DP}$ ), were used to understand the relationship between lightning activity and cloud particle information.

Prior to using radar data, several quality control procedures were performed to ensure the reliability of the data. The Lidar Radar Open Software Environment (LROSE) RadxQc software was applied to correct for precipitation-induced attenuation and to remove terrain or ocean clutters (Bell et al. 2022). Since S-band radar operates at a wavelength with little influence from rain attenuation, the difference in data quality before and after applying quality checks was negligible (not shown). We further filtered out undesired gates using criteria based on  $Z_H$ ,  $\rho_{hv}$ , and the texture of base products. Only data satisfying the following conditions were retained to eliminate outliers:  $Z_H > 0$  dBZ,  $\rho_{hv} > 0.75$ , texture of  $\Phi_{DP} < 20^\circ$ , texture of  $Z_{DR} < 2.5$  dB, texture of  $\rho_{hv} < 0.3$ , and texture of  $Z_H < 8$  dBZ. When coordinate transformations were required, the polar-coordinate-based original data were converted to Cartesian grids using the map sub-module provided by the Python ARM Radar Toolkit (Py-ART) (Helmus and Collis 2016). This module obtains grid points through interpolation of all radar gates within a specified radius of influence, employing either the Cressman or Barnes weighting method (Cressman 1959; Barnes 1964).

The modified hydrometeor classification algorithm (HCA) based on fuzzy logic from Mahale et al. (2014) was used to classify the cloud particle types. This algorithm closely resembles the operational HCA from Park et al. (2009), but with a few simplifications to mitigate the uncertainty of the specific differential phase ( $K_{DP}$ ) and confidence vector calculations. The melting level was estimated from vertical temperature profiles of the 5<sup>th</sup> generation European Centre for Medium-Range Weather Forecasts reanalysis

data and compared with the bright band signatures in the stratiform region. Five radar variables were employed for hydrometeor identification:  $Z_H$ ,  $Z_{DR}$ ,  $\rho_{hv}$ , a texture parameter of the  $Z_H$  field, and a texture parameter of  $\Phi_{DP}$ . Each variable has a specific range of values associated with different types of radar echo, and each range is specified by a trapezoidal weighting function with one as the maximum and zero as the minimum. By adding the different variables multiplied by the weighting function, the HCA can distinguish the radar echo into ten classes: (1) ground clutter and anomalous propagation (GC/AP), (2) biological scatter (BS), (3) dry snow (DS), (4) wet snow (WS), (5) ice crystals (CR), (6) graupel (GR), (7) large drops (BD), (8) light and moderate rain (RA), (9) heavy rain (HR), and (10) a mixture of rain and hail (RH). As radar resolution volumes often contain a mix of various hydrometeors, the final product denotes the most dominant species of hydrometeor. It is important to note that the most dominant species of hydrometeor in the radar observations may not coincide with that in real cloud microphysics state parameters such as mixing ratios.

## 2.3 Automatic Weather Station Observation

Rain gauges from automatic weather station (AWS) networks operated by KMA were used to establish case selection criteria by identifying the initiation and development of the thunderstorm that caused rainfall damage in the SMA on August 8. The storm cells in a multicellular convective system formed and dissipated several times, resulting in large variations in rainfall intensity depending on the growth stages. A 15-min accumulated rainfall was sampled at 5-min intervals to effectively represent the fluctuation in rainfall intensity. The AWS covers over 700 stations nationwide, with twenty-seven stations in Seoul, providing relatively high-resolution precipitation data. The irregularly distributed AWS data were interpolated to a 1 km grid using the Barnes weighting method to fill the gaps in observations (Barnes 1964).

## 3 Overview for the Seoul Flood Episode of August 8, 2022

In this section, we examine the spatial distribution of precipitation and lightning flashes during the Seoul floods, with a special focus on August 8. Rain rate and lightning rate at 5-min intervals were analyzed, and cases were selected for further analysis. Firstly, we explore the synoptic patterns that caused the flooding. Figure 1 displays the surface weather map (a) and the corresponding distributions of the 850-hPa equivalent potential temperature and wind, and the 500-hPa geopotential height (b) of the Korean Integrated Model (KIM) system at 9 LT on August 8. At the surface,

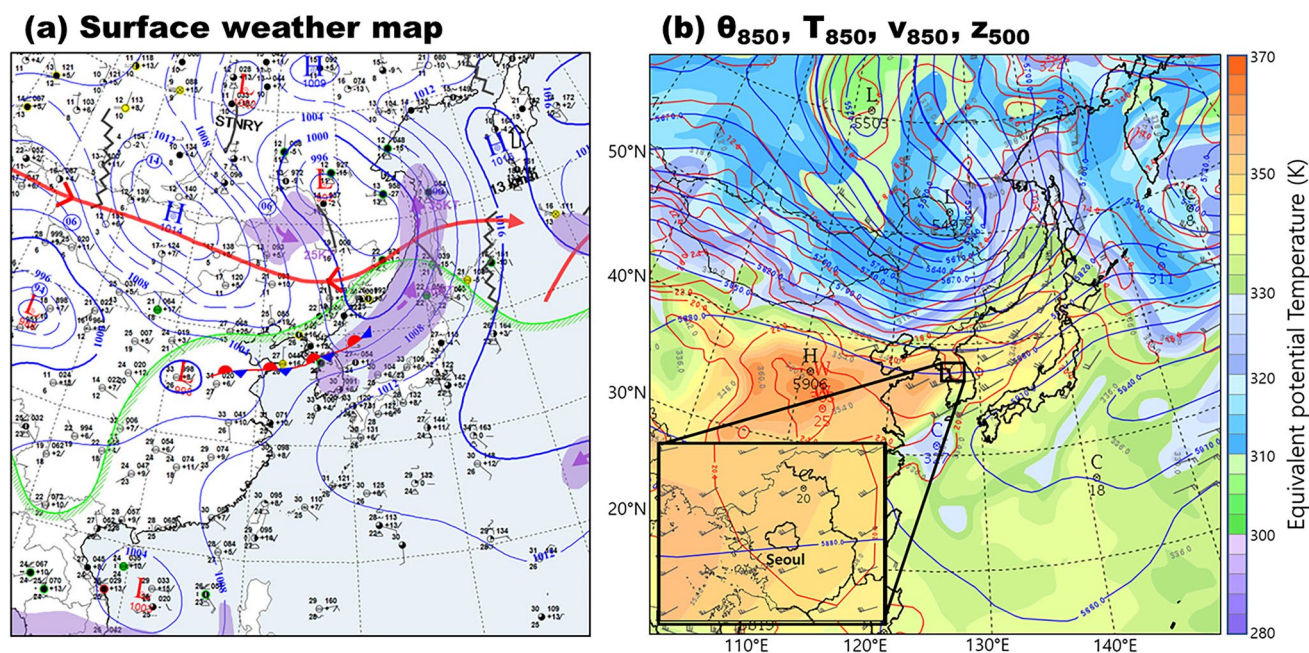


**Fig. 1** **a** Surface weather map and **b** 850-hPa equivalent potential temperature ( $\theta_{850}$  in K, shading), 850-hPa wind ( $V_{850}$  in  $\text{m s}^{-1}$ ,  $\geq 10 \text{ m s}^{-1}$ ), and 500-hPa geopotential height ( $\Phi_{500}$  in gpm, blue contour) from the Korean Integrated Model at 9 LT on August 8,

2022. The red arrow and purple shaded area in the left panel represent upper- and low-level jets, respectively. Seoul and its surroundings are highlighted in an extended map on the right panel

a zonal stationary front was developed over central Korea, with high- and low-pressure systems situated over northern Mongolia and eastern Siberia, respectively (Fig. 1a). The resultant pressure gradient produced northwesterly winds. As the air mass moved southward, it collided with the relatively warm and moist air mass of the western North Pacific subtropical high pressure, resulting in zonal isobars over Korea. The stationary front formed along these isobars. In addition, the proximity of the upper-level jet and the low-level jet during this period further enhanced the kinematic activity near the front, leading to the development of a long-lasting frontal system (Shapiro 1981).

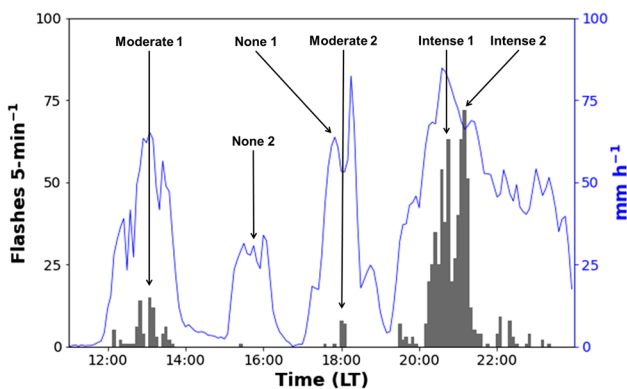
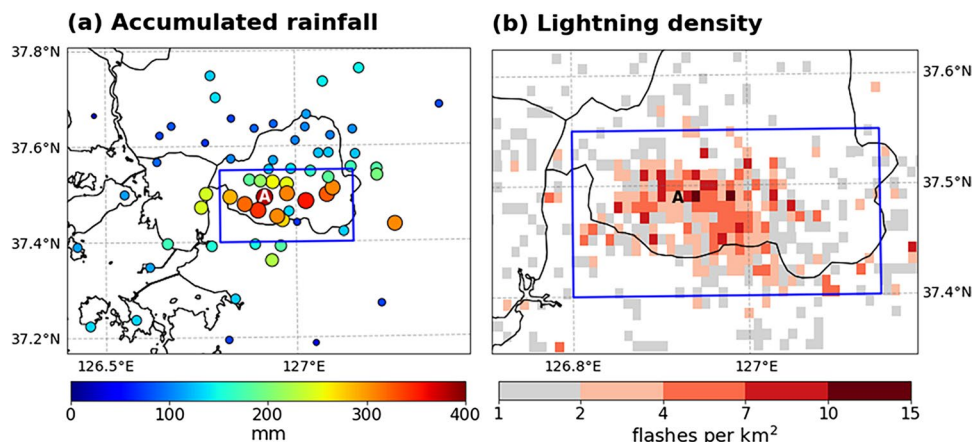
Figure 1b illustrates the lower and middle atmospheric environments driving this stationary front. The edge of the western North Pacific subtropical high extended into central Korea (seen by the 5880 gpm contour on the extended map) and was connected to the low-level jet with strong winds exceeding  $10 \text{ m s}^{-1}$ . This allowed warm and moist air from the Shandong Province in China to move eastward into Korea, serving as a major source of moisture for the front. In contrast, the relatively cold and dry air mass from northern China and western Manchuria was directed southward into Korea by the prevailing low-pressure system over eastern Siberia. The collision of these two air masses of different temperatures created favorable conditions for frontogenesis.

Figure 2 displays the spatial distribution of the accumulated rainfall (a) and lightning density (b) on August 8. A

substantial amount of rain, exceeding 100 mm, was observed throughout the SMA (Fig. 2a). In particular, it rained explosively in the southern region of Seoul. Among the 64 AWS stations presented in this figure, 16 stations located in southern Seoul recorded intense rainfall  $\geq 200 \text{ mm}$ . The maximum daily rainfall reached up to 381.5 mm at the KMA station (marked with A). Notably, there is a significant contrast between the northern and southern regions of the city. The southern region experienced an average rainfall of 252 mm from 16 stations, while the northern region recorded only 112 mm from 11 stations. The study area was defined to encompass southern Seoul, as indicated by the blue box ( $37.35^\circ\text{--}37.62^\circ\text{N}$ ,  $126.7^\circ\text{--}127.2^\circ\text{E}$ ).

Lightning activity, the accumulated number of lightning flashes within a unit area (i.e.,  $1 \text{ km} \times 1 \text{ km}$ ), showed a spatial pattern similar to that of rainfall (Fig. 2b). The lightning density map is magnified to highlight regions with significant concentrations of lightning flashes. The total number of lightning flashes for August 8 was 866, of which 687 flashes (approximately 80% of the total) occurred within the blue box. In particular, lightning was concentrated in the southwestern region of the city, with a peak lightning density of 14 flashes  $\text{km}^{-2}$  in the vicinity of marked A, where the daily rainfall reached its maximum. It is worth mentioning that this unusual lightning activity occurred only on August 8 and no lightning was recorded on August 9, despite the abundant rainfall over the two consecutive days. On August

**Fig. 2** Distributions of (a) the accumulated rainfall at 64 AWS locations (27 inside Seoul and 37 in the surrounding regions) and (b) the lightning density on August 8, 2022. The circle size of (a) is proportional to the accumulated rainfall, and the marked A indicates the KMA station. The spatial domain of each figure is arbitrary, and the following analysis is limited to the region of the blue box



**Fig. 3** Time series of lightning rate (bar, left y-axis) and maximum rain rate (blue line, right y-axis) within the box area in Fig. 2 on August 8, 2022. The corresponding cases listed in Table 1 are indicated

9, the overall atmospheric environment was not conducive to lightning, as the potential energy available for convection decreased, and cloud heights were relatively lower (not shown).

The severe flooding and lightning in Seoul were attributed to multicell storms consisting of constantly evolving and dissipating convective cells. The fluctuating rainfall and lightning activity made it difficult to capture a representative instance of the storms. Therefore, we analyzed the

time series of rainfall and lightning activity for August 8. Figure 3 displays the lightning rate (flashes 5-min<sup>-1</sup>) and the maximum rain rate (mm h<sup>-1</sup>) over the analysis area (see blue box region in Fig. 2) at 5-min intervals from 11 to 24 LT on August 8. The hourly rain rate was estimated by multiplying the 15-min rain totals from AWS by four. The rain rate and lightning rate exhibit abrupt temporal variations, based on which four distinct periods were categorized. Each period presents variations in rainfall and lightning intensity. During the most intense periods after 20 LT, the lightning rate of > 70 flashes 5-min<sup>-1</sup> was observed with a rain rate of up to 85 mm h<sup>-1</sup>. In contrast, only a few lightning flashes were detected between 15–17 LT, when the maximum rain rate remained < 40 mm h<sup>-1</sup>. There appears to be a potential positive correlation between the rain rate and lightning rate. However, it is uncertain whether there is a clear linear relationship between these two variables. At approximately 18 LT, the lightning rate barely exceeded 10 flashes 5-min<sup>-1</sup>, despite rainfall peaking at over 80 mm h<sup>-1</sup>.

For a more detailed analysis of the storms, we selected six cases based on their lightning rate: two cases each from the categories of intense, moderate, and none (noted in Fig. 3). Table 1 provides a summary of these cases, including information on the lightning rates and rain rates within a given domain. The domain was determined by dividing a region with a high concentration of lightning flashes or heavy rainfall into smaller sections. The data shows that

**Table 1** Selected cases for a comparative analysis on August 8, 2022

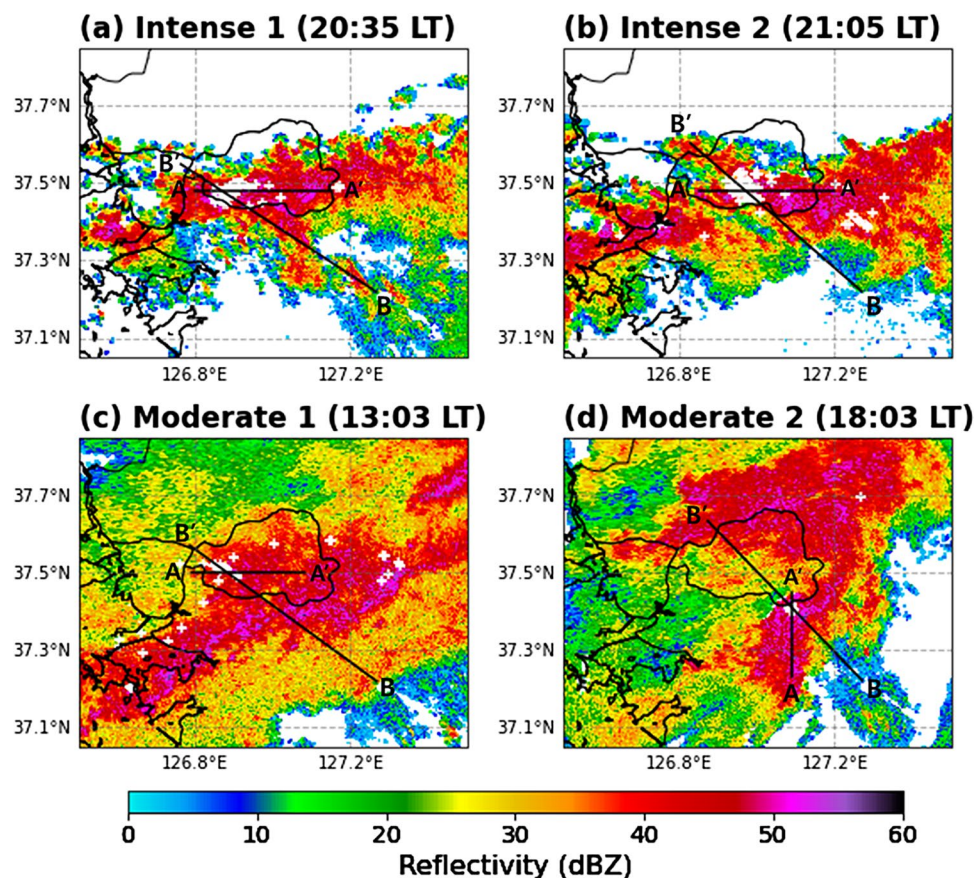
Lightning activity	Time (LT)	Lightning rate (flashes 5-min <sup>-1</sup> )	Rain rate (mm h <sup>-1</sup> )	Domain
intense 1	20:35–20:40	63	81	126.82°–126.99°E, 37.45°–37.53°N
intense 2	21:05–21:10	72	66	126.88°–127.05°E, 37.45°–37.53°N
moderate 1	13:00–13:05	15	65	126.81°–126.93°E, 37.47°–37.54°N
moderate 2	18:00–18:05	12	53	127.06°–127.14°E, 37.38°–37.44°N
none 1	17:40–17:45	-	64	126.84°–126.95°E, 37.41°–37.56°N
none 2	15:35–15:40	-	29	127.01°–127.12°E, 37.50°–37.60°N

cases with high lightning rates have, on average, higher rain rates. For instance, the intense cases with  $> 60$  lightning flashes recorded an average rain rate of  $74 \text{ mm h}^{-1}$ , while the moderate cases with slightly more than 10 lightning flashes have a lower rain rate of  $59 \text{ mm h}^{-1}$ , and cases with no recorded lightning activity have the lowest average rain rate of  $47 \text{ mm h}^{-1}$ . However, the individual cases of intense 2, moderate 1, and none 1 showed different trends. Their lightning rates varied from 0 to  $72 \text{ flashes } 5\text{-min}^{-1}$  despite having similar rain rates of approximately  $65 \text{ mm h}^{-1}$ . These results suggest that a consistent relationship between lightning rate and rain rate may not exist at a smaller spatiotemporal scale.

The spatial pattern of lightning locations also varied with lightning activity. To visually represent these locations, we plotted them on reflectivity position indicator maps (Fig. 4). The time information for the radar data used in this figure was selected from either the observation time included in the periods listed in Table 1 or from the closest available time due to the irregular time intervals in radar observations. Figure 4a displays more than 60 lightning flashes within a small area in the southwestern part of

Seoul (around  $126.9^\circ\text{E}$  and  $35.5^\circ\text{N}$ ) during the intense 1 case. This intense activity continued even at 21:05 LT, with more than 70 lightning flashes observed within areas of comparable size (Fig. 4b). However, as the lightning intensity decreased, changes in the spatial distribution of the lightning were observed. Unlike the clustered patterns of the intense cases, the lightning during the moderate 1 case was scattered (Fig. 4c); although the lightning area was similar to that of the intense cases, the number of lightning flashes significantly reduced, with only 15 flashes recorded. In the moderate 2 case, although lightning occurred in clusters, the area was relatively smaller (Fig. 4d). These observations suggest a possible relationship between the intensity of lightning activity and the spatial distribution of its occurrences. For further radar analysis, arbitrary lines such as A-A' and B-B' were drawn, passing through the central regions of lightning events. The lines in cases without lightning were determined based on the precipitation regions (not shown). The detailed analysis for these two lines is shown in Figs. 7 and 9.

**Fig. 4** Reflectivity factor (shading) at horizontal polarization with a  $1.3^\circ$  elevation angle and the location of lightning flashes (white cross) for (a), (b) intense, and (c) and (d) moderate of the cases listed in Table 1. The cross sections of two lines (A-A' and B-B') are examined in Figs. 7 and 9



## 4 Variation of Cloud Hydrometeors with Lightning Activity

### 4.1 Time Lag Between Graupel Formation and Lightning Event

The microphysical properties inside the clouds were investigated using polarimetric radar data to examine the differences among the selected cases, with a particular emphasis on the temporal and spatial behaviors of cloud hydrometeors in relation to lightning activity. Firstly, the temporal correlation between the formation of graupel and the occurrence of lightning was investigated. Figure 5 shows the temporal variations of lightning rate and graupel volume above the temperature heights of 0 °C and –10 °C within the study domain outlined in Fig. 2. To analyze the correlation between the formation of graupel and the occurrence of lightning, we focused on a multicellular storm containing the intense cases. The graupel volume was calculated by adding the volumes of all the pixels classified as ‘GP’ by the HCA algorithm, assuming similar amounts of graupel exist in those pixels.

In Fig. 5, it was found that the temporal behavior of the lightning activity had a closer relationship to the graupel volume above the –10 °C layer compared to the 0 °C layer. The lightning activity, which first appeared at around 19:30 LT and persisted for over two hours, was accompanied by a temporal fluctuation with notable peaks at 20:23, 20:35, and 21:05 LT. The behavior of the graupel volume above the –10 °C layer also showed three peaks that followed a similar trend to the lightning, with the location coinciding with or slightly preceding the lightning rate peaks by a time-stamp of approximately 6 min. The

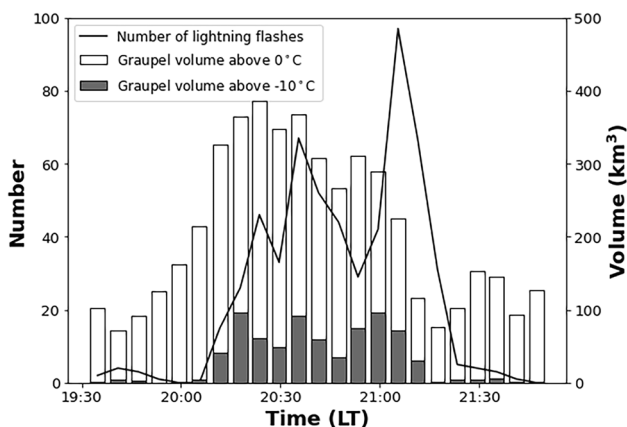


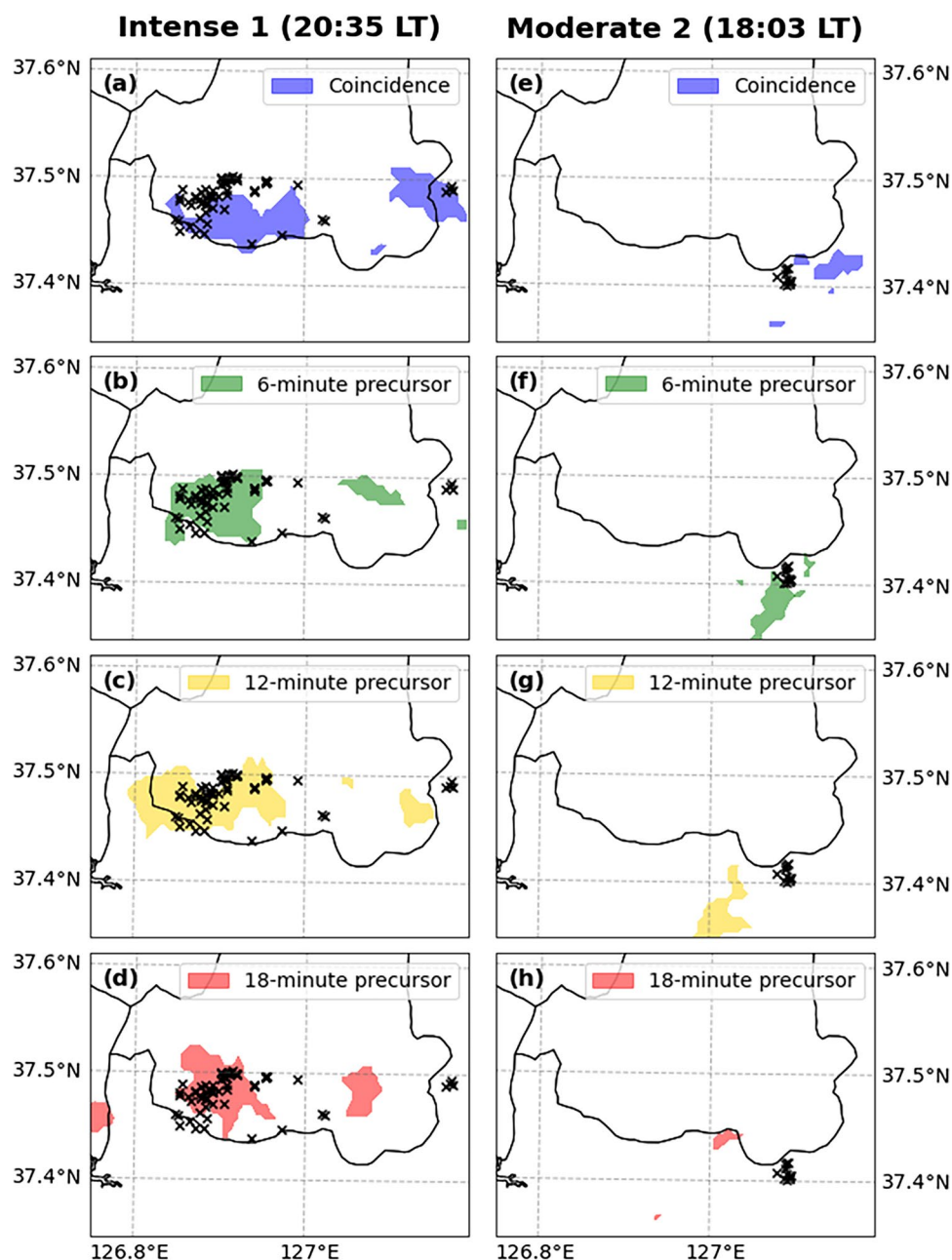
**Fig. 5** Time series of lightning rate (line, left y-axis) and graupel volume above the two different temperature layers, 0 °C (white bar, right y-axis) and –10 °C (gray bar, right y-axis), within the box area in Fig. 2 for the period of 19:30–21:50 LT on August 8, 2022

reduced graupel volume even corresponded to a reduction in lightning activity. However, the graupel volume above the 0 °C layer did not display distinct peaks during the period of intense lightning but instead exhibited a sudden increase after the lightning had dissipated.

To quantitatively assess the relationship between lightning rate and graupel volume above the 0 °C and –10 °C layers, we calculated the Pearson correlation coefficients ( $R_0$  and  $R_{-10}$ , respectively) and analyzed the variations of the coefficients as a function of the time lag between them. Using time-synchronized data, the  $R_0$  and  $R_{-10}$  were found to be 0.33 and 0.59, respectively; only the  $R_{-10}$  was found to be statistically significant at the 95% confidence level. However, recalculation of  $R_0$  and  $R_{-10}$  using graupel volumes collected approximately 6 min prior to the lightning events resulted in significantly increased coefficients of 0.67 and 0.87, respectively (both significant at the 99% confidence level). The coefficients then decreased with increasing lead time. This implies a delay of about 6 min between the formation of graupel above the –10 °C layer and the first lightning flashes. The reduced influence of graupel above the 0 °C layer can be attributed to the presence of liquid water surrounding its surfaces, which is a result of the relatively warm temperatures (–3 °C to –8 °C). Note that wet graupel creates unfavorable conditions for lightning generation (Emersic et al. 2011).

The time lag was also confirmed by comparing the evolution of the graupel area in the –10 °C layer with the locations of lightning flashes in Fig. 6. The graupel areas corresponding to different times were distinguished by color: blue, green, yellow, and red, representing 0, 6, 12, and 18 min prior to the lightning event, respectively. In the southwestern region (around 126.9°E) shown in Fig. 6a–d, where the horizontal displacement of the graupel area over time was relatively small, the shape of the green area (i.e., 6 min time lag) most closely matched the lightning location. Most of the lightning flashes were distributed throughout the entire green area, although some exceptional lightning flashes were observed outside of this region. A similar feature was observed in the moderate 2 case (Fig. 6e–h). Even though concentrated lightning flashes in the southeast region outside of Seoul were not included in the green area, they were still closely distributed. In both the intense 1 and moderate 2 cases, other color areas (i.e., blue, yellow, and red) with different time delays did not correspond well to the lightning. It should be noted, however, that the formation of graupel alone does not account for all lightning activity. The movement of the cloud system and the influence of different types of cloud particles could be factors contributing to the scattered locations of lightning flashes.

**Fig. 6** Distribution of lightning flashes (cross) and graupel area (shading) in (a)–(d) intense 1 and (e)–(h) moderate 2 case. The graupel area is shown in different colors up to 18 min at 6-min intervals prior to the corresponding lightning events (20:35 and 18:03 LT). Note that the lightning locations are fixed



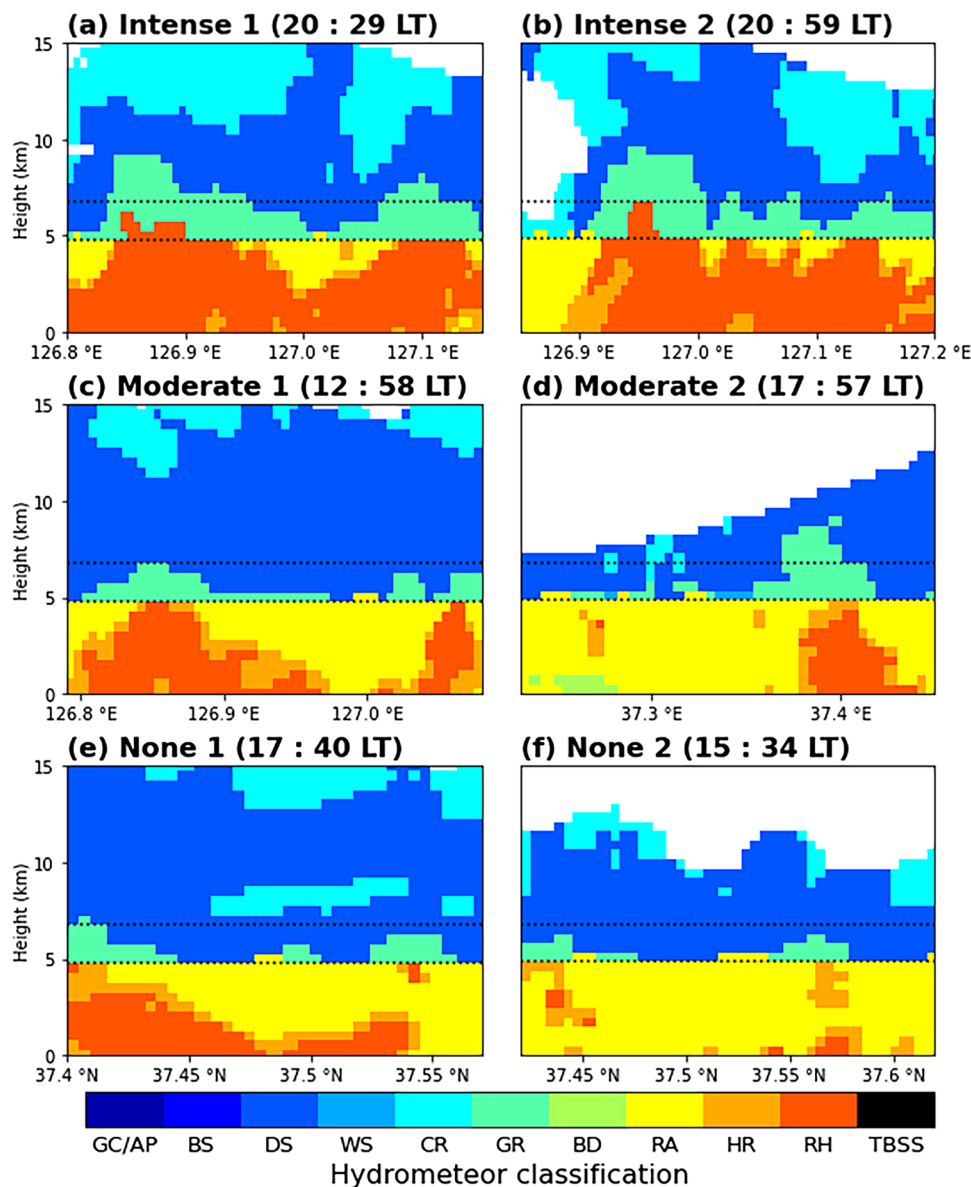
## 4.2 Vertical Distribution of Hydrometeors and Their Polarimetric Signatures

In this section, we examine the properties of the HCA vertical distribution and the base products, such as  $Z_H$ ,  $Z_{DR}$ , and  $\rho_{HV}$ , of the radar observations to identify the microphysical characteristics of the lightning-prone regions. In order to account for the time lag between graupel formation and lightning occurrence, the time stamp for the radar data is set to 6 min prior to the radar reflectivity and lightning observation data. First, the vertical arrangement of the HCA products along the line A–A' in Fig. 4 for each case is presented in Fig. 7. In the intense cases, the lightning locations

appeared densely concentrated in specific small areas, around 126.8°–126.9°E in the intense 1 and 126.9°–127°E in the intense 2 (Fig. 4a and b). These areas corresponded closely to the areas where graupel particles were transported upward to high altitudes above the  $-10$  °C temperature level (approximately 7 km) and also exhibited sufficient ice crystals in the upper layer above 10 km height (Fig. 7a and b). Such microphysical patterns are thought to be conducive to lightning generation, as the electrical charge separation in thunderstorms is mainly due to charge transfer between graupel and smaller ice crystals. In addition, rain or hail (hereafter referred to as 'RH') was observed just above the melting layer (approximately 5 km) within lightning-prone



**Fig. 7** Vertical cross sections of hydrometeor classification algorithm (HCA) products along the line A–A' shown in Fig. 4 for (a) and (b) intense, (c) and (d) moderate, and (e) and (f) none cases. Two dotted lines align with the temperature levels of 0°C (lower line) and –10°C (upper line). The time stamps for the HCA data of the intense and moderate cases are 6 min prior to the reflectivity map of Fig. 4



regions. The RH class could be detected by either supercooled liquid water or wet graupel being lifted by strong updrafts. This observation may be related to a notable polarimetric signature, the  $Z_{DR}$  column, which often appears as a columnar region of enhanced  $Z_{DR}$  due to a mixture of large liquid droplets, graupel, and sometimes small hail above the melting layer (MacGorman et al. 2008; Kumjian et al. 2014; Snyder et al. 2015; Zhao et al. 2020; Shrestha et al. 2021). The detection of such features implies the existence of robust updrafts, which are necessary to generate intense lightning.

Figure 7a also shows that both microphysical and kinematic properties must be satisfied for lightning to occur. Comparing the area around 126.9°E and 127.1°E in Fig. 7a, it is clear that both regions fulfill the microphysical conditions conducive to lightning production: graupel above 7 km height and ice crystals in the upper layer. Nevertheless,

lightning activity was only observed in the former region. This observation suggests that additional influencing factors, such as updraft strength, should be considered. Since lightning typically exhibits characteristics of high flash density and smaller flash area in regions of strong updraft (Thiel et al. 2020), it can be inferred that robust updraft was likely present only around 126.9°E.

Similar characteristics were observed in the moderate cases (Fig. 7c and d). In the moderate 1 case, graupel was observed ascending to altitudes up to 7 km, and ice crystals were primarily present in the upper layer limited to the lightning zone (126.8°–126.9°E). In the moderate 2 case, graupel reached an even higher altitude of 10 km, although the existence of ice particles in the upper layers could not be confirmed due to radar range limitations. In contrast, graupel was predominantly distributed at lower altitudes in most

regions of none cases (Fig. 7e and f), resulting in the absence of lightning activity. Despite the graupel particles ascending to higher altitudes above the  $-10\text{ }^{\circ}\text{C}$  layer near the  $37.40^{\circ}\text{N}$  location in Fig. 7e, no lightning activity was recorded. The lack of ice crystals could explain the absence of lightning events, possibly compounded by weak turbulence. According to Mareev and Dementyeva (2017), the effect of turbulence on charge separation mechanisms, influenced by interactions at the hydrometeor-scale, could locally intensify the existing electric fields, potentially triggering lightning.

The radar measurement volume contains a mixture of various hydrometeors, even within a single pixel, while the HCA products indicate the most representative types of hydrometeors in a pixel. Therefore, the base products were analyzed to understand the different possibilities of particle distribution within the cloud. Figure 8 displays box plots showing the vertical variations of the polarimetric variables. A box plot displays the median value as a black line inside the box and the mean as a blue diamond marker, and the box limits represent the 25<sup>th</sup> and 75<sup>th</sup> percentiles. The vertical axis of the plot represents temperature information for different layers, ranging from  $0\text{ }^{\circ}\text{C}$  at an altitude of 5 km to  $-65\text{ }^{\circ}\text{C}$  at 15 km. There are also three boundaries at temperatures of  $-10$ ,  $-20$ , and  $-40\text{ }^{\circ}\text{C}$ , corresponding to altitudes of 7, 9, and 12 km, respectively.

The most notable differences between lightning categories were observed in the temperature range of  $0\text{ }^{\circ}\text{C}$  to  $-10\text{ }^{\circ}\text{C}$ . As lightning activity intensified, the median value of  $Z_H$  increased from 29 to 43 dBZ (Fig. 8a). Note that higher  $Z_H$  values indicate a higher concentration of large particles. When conditions lead to  $Z_H > 40\text{ dBZ}$ , the particle type can be inferred from the corresponding  $Z_{DR}$  values.

$Z_{DR}$ , defined as the logarithmic reflectivity factors at horizontal and vertical polarizations, provides information about the reflectivity-weighted shape of the targets.

In Fig. 8b, the median and mean values of  $Z_{DR}$  of this layer remained close to zero ( $0.1\text{--}0.4\text{ dB}$ ), which can be attributed to the prevalence of spherical-shaped rimmed particles such as graupel and hail (Kumjian 2013). However,  $Z_{DR}$  below the 25<sup>th</sup> percentile in the intense lightning category demonstrated a lower value, with a minimum of  $-1.2\text{ dB}$ . This observation implies the presence of conical-shaped graupel; most hydrometeors, whether in both liquid and solid type, tend to have positive  $Z_{DR}$  values, with the exception of conical-shaped graupel and ice aggregates (Straka et al. 2000; Dolan and Rutledge 2009; Zhao et al. 2022). In environments characterized by strong updrafts, graupel is more likely to form compared to ice aggregates. In addition,  $Z_{DR} > 0.5\text{ dB}$  indicates the presence of liquid water droplets. In general,  $Z_{DR}$  values increase with the size of liquid droplets because their oblate shape causes a substantial phase shift in the horizontal polarization wave compared to the vertical polarization wave. Thus, a high  $Z_{DR}$  indicates the existence of supercooled liquid droplets or wet graupel. This observation was supported by  $\rho_{hv}$  lower than 0.97 (Fig. 8c). It is noted that  $\rho_{hv}$  tends to decrease when different types and shapes of particles, such as dry graupel, wet graupel, and supercooled liquid droplets, are mixed.

The polarimetric signature of graupel, characterized by a high  $Z_H$  above 40 dBZ and low  $Z_{DR}$ , extended to altitudes with temperatures below  $-10\text{ }^{\circ}\text{C}$ , especially for the intense category. In the temperature range of  $-10\text{ }^{\circ}\text{C}$  to  $-20\text{ }^{\circ}\text{C}$ , the 90<sup>th</sup> percentile of  $Z_H$  of the intense category was 41 dBZ, with a median  $Z_{DR}$  value close to zero. Although the

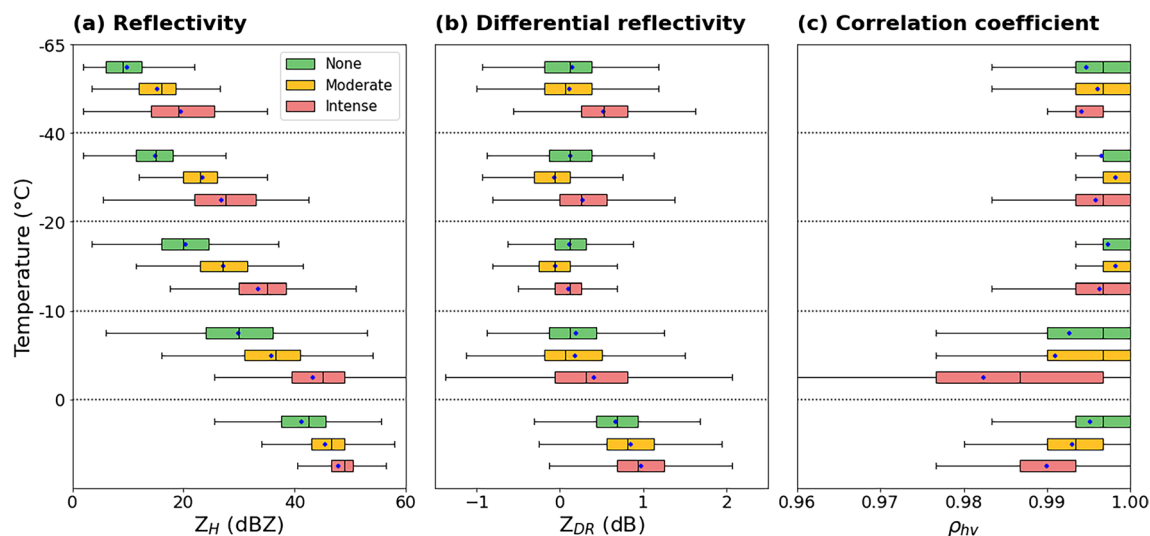


**Fig. 8** Box plots describing polarimetric radar variables including reflectivity, differential reflectivity, and correlation coefficient, for three lightning categories: intense (red), moderate (yellow), and none

(green) listed in Table 1. The boxes represent the quartiles of the dataset, and the mean value is indicated by the blue diamond

moderate category occasionally showed instances where  $Z_H$  values exceeded 40 dBZ, the 99<sup>th</sup> percentile remained below this threshold value (i.e., 40 dBZ). These observations indicate that graupel, which ascends to higher altitudes specifically at temperatures below  $-10$  °C, was predominantly observed in the intense lightning category, suggesting a strong association between graupel height and lightning intensity.

The glaciated layer, with temperatures below  $-20$  °C, primarily consisted of ice particles such as dry snow and pristine ice crystals. Compared to pristine ice crystals, dry snow particles generally exhibit lower  $Z_{DR}$  (Straka et al. 2000). This lower  $Z_{DR}$  is attributed to several factors specific to dry snow, including its small size, low density, and nearly spherical shape. On the other hand, the  $Z_{DR}$  of ice crystals can vary widely depending on their shape and orientation when ice crystals are the major contributor to radar reflectivity. In the upper part of the glaciated layer, the median value of  $Z_{DR}$  was higher than in the lower part (Fig. 8b), suggesting that pristine ice crystals were the dominant hydrometeors in the extremely cold temperature range of  $-40$  °C to  $-65$  °C, while dry snow was mixed in the somewhat warmer temperature range of  $-20$  °C to  $-40$  °C. Additionally, the  $Z_H$  value was higher for the intense lightning category compared to the moderate category (Fig. 8a). This could indicate a higher concentration of hydrometeors or larger particle sizes during more intense storm conditions.

Ice particles within a thunderstorm can align themselves due to the influence of electric fields, and their alignment direction can be inferred from  $\Phi_{DP}$ , which represents the total phase difference between received horizontally and vertically polarized waves.  $\Phi_{DP}$  is affected by propagation effects along the entire radar path, and the derivative of  $\Phi_{DP}$  along the radar range determines the direction of alignment. Figure 9 illustrates the propagation of radar measurements, including  $\Phi_{DP}$ ,  $Z_{DR}$ ,  $Z_H$ , and  $\rho_{hv}$ , along the radar beam direction (solid lines B-B' in Fig. 4). The lines were strategically chosen to pass through the center of the corresponding lightning domains. Histograms of lightning locations over the specific area listed in Table 1 are also presented as a bar plot as a function of distance from the radar point.

The most prominent feature in Fig. 9 is the slope of  $\Phi_{DP}$ , which extends along the radar range. The decrease in  $\Phi_{DP}$  is observed at a range of approximately 35–49 km in the intense 1 case and 47–58 km in the moderate case (Fig. 9a and f). The corresponding heights for these ranges are approximately 11–14.8 km in the intense 1 case and 10–12.1 km in the moderate case. In these regions,  $Z_H$  and  $\rho_{hv}$  consistently displayed values exceeding 15 dBZ and 0.98, respectively (Fig. 9b and g). High  $Z_H$  and  $\rho_{hv}$  at altitudes above 10 km with low temperatures indicate a high concentration of ice crystals. In such an environment, a negative shift of  $\Phi_{DP}$  can be interpreted as a result of the vertical alignment of

ice particles. When the average geometrical projection of crystals in the vertical direction exceeds that in the horizontal direction, the  $\Phi_{DP}$  decreases with the slant range during the alternate transmission and reception of horizontally and vertically polarized waves (Hendry and McCormick 1976; Caylor and Chandrasekar 1996; Ryzhkov and Zrnić 2007; Hubbert et al. 2014). The presence of lightning within the range of 41–49 km in the intense 1 and 45–54 km in the moderate 1 also supports the arrangement of ice particles, as electric fields tend to align vertically in typical thunderstorms accompanied by lightning (Fig. 9e and j).

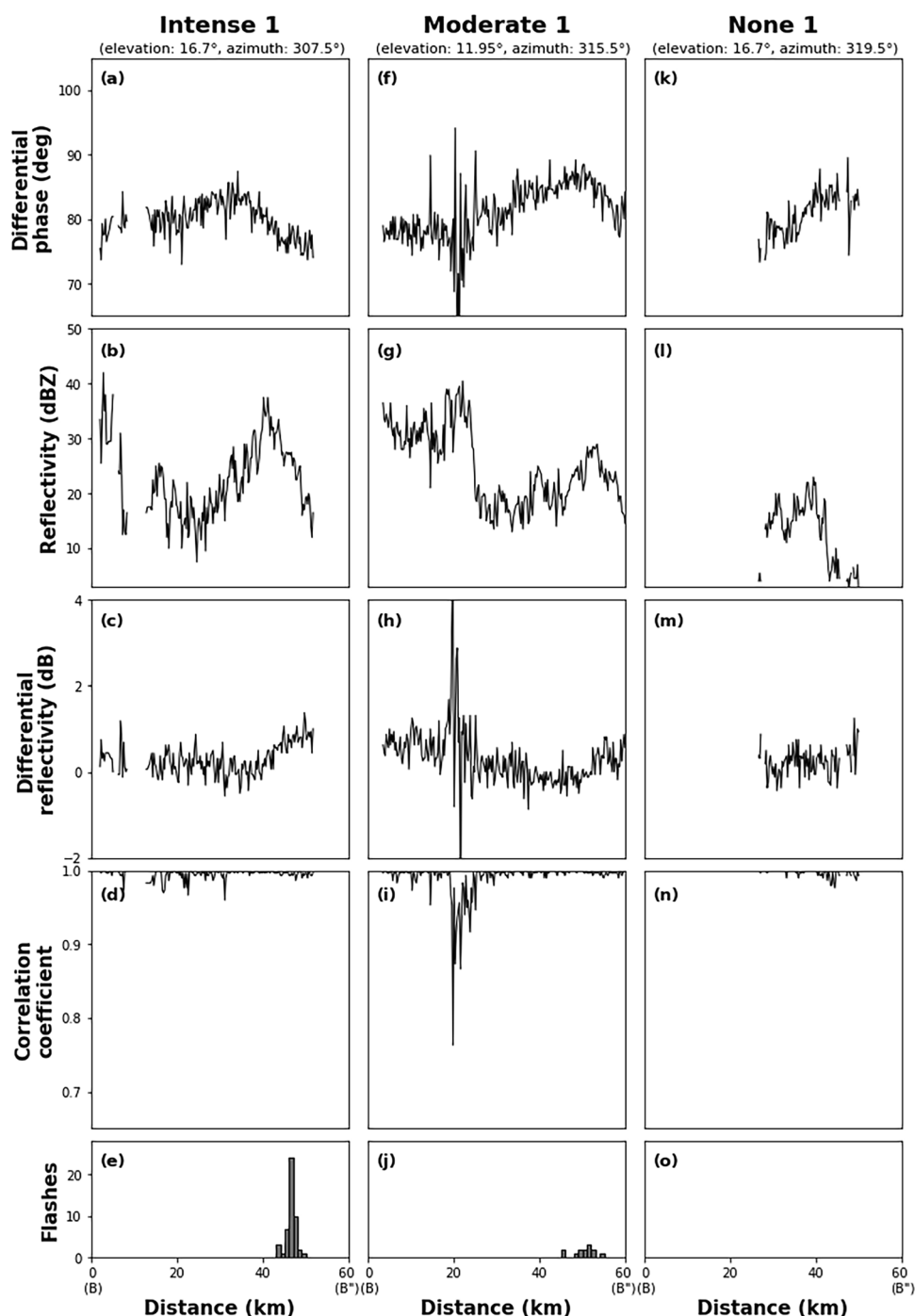
Vertically aligned ice particles also influence the  $Z_{DR}$  sign alongside variations in the effective lengths of the ice particles due to orthogonally polarized electric fields. This vertical alignment leads to negative  $Z_{DR}$  values. However, near-zero or slightly positive  $Z_{DR}$  were observed around the lightning zone (Fig. 9c and h). This unexpected result can be understood by considering the geometric characteristics of ice crystals. At extremely cold temperatures below  $-20$  °C, ice crystals typically take on columnar or plate-like structures (Houze 2014), which respond differently to a strong electric field. The columnar ice crystals align themselves with their major axis perpendicular to the direction of the electric field, causing a vertical alignment and consequently resulting in a negative  $Z_{DR}$ . In contrast, plate-like ice crystals align with their major axis perpendicular to the electric field, resulting in a horizontal orientation due to their shape. This alignment pattern results in  $Z_{DR}$  values that are close to zero or slightly positive.

In summary, the decrease in  $\Phi_{DP}$  and the near-zero  $Z_{DR}$  values suggest the possibility of the coexistence of vertically aligned columnar ice crystals and randomly oriented plate-like ice crystals. This conclusion is supported by Hubbert et al. (2014), who demonstrated that a decrease in  $\Phi_{DP}$ , accompanied by near-zero  $Z_{DR}$  values, indicates the presence of different types of ice crystals, where smaller aligned ice crystals contribute to the  $K_{DP}$  signatures, and larger aggregates or graupel contribute to the  $Z_{DR}$  signatures.

## 5 Concluding Remarks

In this study, we conducted an in-depth analysis of HCA products and polarimetric signatures to gain insight into the temporal and spatial evolution of cloud hydrometeors within thunderstorms and their direct correlation with lightning occurrence. Figure 10 provides a comprehensive understanding of the key factors influencing lightning activity. The most significant finding centers on the critical role that the presence of dry graupel, particularly at altitudes of temperatures below  $-10$  °C, plays in the initiation of lightning events. Dry graupel was identified by high  $Z_H > 40$  dBZ and negative or near-zero  $Z_{DR}$  values in the

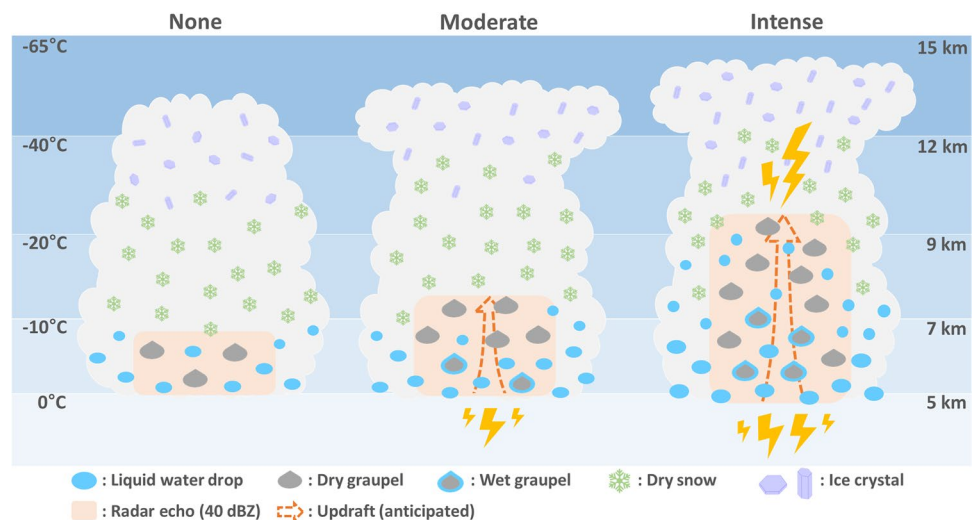
**Fig. 9** Measurements of differential phase, reflectivity, differential reflectivity, and correlation coefficient (a)–(d) along the 16.7° elevation and 307.5° azimuth angles in the intense 1 case, (f)–(i) the 11.95° elevation and 315.5° azimuth angles in the moderate 1 case, and (k)–(n) the 16.3° elevation and 319.5° azimuth angles in the none 1 case. The beam direction is indicated by solid black line B-B' in Fig. 4. (e), (j), and (o) represent the histograms of lightning flashes over the specific domain listed in Table 1, which are plotted as a function of distance from the radar point (marked with B in Fig. 4)



region prone to lightning activity. It is worth noting that the presence of graupel above  $-10^{\circ}\text{C}$  occurred approximately 6 min before lightning was observed. Considering that flash floods usually endure for less than 90 min (Haerter et al. 2010; Westra et al. 2014; Merz and Blöschl 2003), and that hourly extreme rainfall events can result in substantial damage (Kim et al. 2023), a 6-min interval could potentially serve as a significant precursor.

In cases of intense lightning, we observed the concurrent presence of liquid water and graupel just above the melting layer, which was identified by the column-shaped RH criteria in the HCA products. This RH pattern can be interpreted as either supercooled liquid water lifted by strong updrafts or wet graupel surrounded by a liquid water shell. While the existence of ice crystals is highly likely under such conditions, their signals might be masked by larger particles,

**Fig. 10** Conceptual illustration of the vertical distribution of hydrometeors and polarimetric signature in storms with different lightning activities including none, moderate, and intense



underscoring the need for further investigation. Moreover, a significant polarimetric signature relates to the reduction in  $\Phi_{DP}$  observed in regions with high  $Z_H > 15$  dBZ and slightly positive or near-zero  $Z_{DR}$  in the upper levels of the cloud. These signatures are associated with a high concentration of vertically aligned ice crystals, particularly columnar and plate-like shapes.

The generation of lightning is widely understood to result from charge separation caused by collisions between cloud particles, such as graupel and ice crystals. To fully understand this process, it is essential to study not only the types and distributions of cloud particles but also the underlying kinematics that drive particle collisions. However, the present study faced a limitation due to the lack of kinematics information, primarily caused by the scarcity of radar observations needed to generate three-dimensional wind fields. Obtaining high-quality wind retrievals with sufficient resolution for cloud analysis requires proper positioning and spacing of radar observing sites, which are currently lacking even in the SMA region. In Fig. 10, we depict the expected updraft information with an orange-dashed arrow based on previous research on updrafts and lightning (Solomon and Baker 1998; Wiens et al. 2005; Deierling and Petersen 2008; Schultz et al. 2017; Stough et al. 2022). These studies have shown that an updraft volume of  $\geq 10 \text{ m s}^{-1}$  (the value may vary between studies) above the melting layer is a more favorable condition for lightning occurrence compared to considering the maximum or average velocity (Deierling and Petersen 2008).

The present study provides valuable information on the microphysical characteristics of thunderstorms and their influence on lightning activity. The type of cloud hydrometeors and their shape and orientation in regions prone to lightning were explored by performing in-cloud analysis

using dual-polarization radar. Considering the increasing frequency of heavy rainfall during the summer season in Korea (e.g., Ho et al. 2003; Kim et al. 2006; Chang et al. 2023), this result can provide crucial information for proactive management of lightning events and other severe weather conditions associated with lightning, such as torrential downpours. To accomplish this objective, it is essential to examine a broader range of cases to draw concrete conclusions. This will allow for a deeper understanding of cloud characteristics under diverse environmental conditions that can trigger lightning. Additionally, efforts should be directed toward enhancing the accuracy and reliability of radar-retrieved data for a more accurate assessment of in-cloud microphysical species' behaviors.

**Funding** This work was funded by the Korea Meteorological Administration Research and Development Program (Grant RS-2023-00236880). We acknowledge the critical comments from anonymous reviewers and editor.

## Declarations

**Conflict of Interest** The authors declare that they have no conflict of interest.

**Open Access** This article is licensed under a Creative Commons Attribution 4.0 International License, which permits use, sharing, adaptation, distribution and reproduction in any medium or format, as long as you give appropriate credit to the original author(s) and the source, provide a link to the Creative Commons licence, and indicate if changes were made. The images or other third party material in this article are included in the article's Creative Commons licence, unless indicated otherwise in a credit line to the material. If material is not included in the article's Creative Commons licence and your intended use is not permitted by statutory regulation or exceeds the permitted use, you will need to obtain permission directly from the copyright holder. To view a copy of this licence, visit <http://creativecommons.org/licenses/by/4.0/>.

## References

- Barnes, S.L.: A technique for maximizing details in numerical weather map analysis. *J. Appl. Meteor. Climatol.* **3**, 396–409 (1964)
- Bell, M.M., Dixon, M., Lee, W.-C., Javornik, B., DeHart, J., Cha, T.-Y., DesRosiers, A.: nsf-Irose/Irose-topaz: Irose-topaz stable final release 20220222 (Irose-topaz-20220222). Zenodo (2022). <https://doi.org/10.5281/zenodo.6909479>
- Betz, H.-D., Schmidt, K., Oettinger, P., Wirz, M.: Lightning detection with 3-D discrimination of intracloud and cloud-to-ground discharges. *Geophys. Res. Lett.* (2004). <https://doi.org/10.1029/2004GL019821>
- Betz, H.-D., Marshall, T.C., Stolzenburg, M., Schmidt, K., Oettinger, W.P., Defer, E., Konarski, J., Laroche, P., Dombai, F.: Detection of in-cloud lightning with VLF/LF and VHF networks for studies of the initial discharge phase. *Geophys. Res. Lett.* (2008). <https://doi.org/10.1029/2008GL035820>
- Betz, H.-D., Schmidt, K., Laroche, P., Blanchet, P., Oettinger, W.P., Defer, E., Dziewit, Z., Konarski, J.: LINET—An international lightning detection network in Europe. *Atmos. Res.* **91**, 564–573 (2009)
- Caylor, I., Chandrasekar, V.: Time-varying ice crystal orientation in thunderstorms observed with multiparameter radar. *IEEE Trans. Geosci. Remote Sens.* **34**, 847–858 (1996)
- Chang, M., Ho, C.H., Ho, J., Cha, E.J.: Centennial analysis in tropical cyclone-induced precipitation in Korea. *Weather Clim. Extremes* **39**, 100549 (2023). <https://doi.org/10.1016/j.wace.2023.100549>
- Cressman, G.P.: An operational objective analysis system. *Mon. Weather Rev.* **87**, 367–374 (1959)
- Deierling, W., Petersen, W.A., Latham, J., Ellis, S., Christian, H.J.: The relationship between lightning activity and ice fluxes in thunderstorms. *J. Geo. Res. Atmos.* (2008). <https://doi.org/10.1029/2007JD009700>
- Deierling, W., Petersen, W.A.: Total lightning activity as an indicator of updraft characteristics. *J. Geo. Res. Atmos.* (2008). <https://doi.org/10.1029/2007JD009598>
- Dolan, B., Rutledge, S.A.: A theory-based hydrometeor identification algorithm for X-band polarimetric radars. *J. Atmos. Ocean. Technol.* **26**, 2071–2088 (2009)
- Emsic, C., Heinselman, P.L., MacGorman, D.R., Bruning, E.C.: Lightning activity in a hail-producing storm observed with phased-array radar. *Mon. Weather Rev.* **139**, 1809–1825 (2011)
- Haerter, J.O., Berg, P., Hagemann, S.: Heavy rain intensity distributions on varying time scales and at different temperatures. *J. Geophys. Res. Atmos.* **115** (2010). <https://doi.org/10.1029/2009JD013384>
- Helmus, J.J., Collis, S.M.: The Python ARM Radar Toolkit (Py-ART), a library for working with weather radar data in the Python programming language. *J. Open Res. Softw.* **4**, e25 (2016). <https://doi.org/10.5334/jors.119>
- Hendry, A., McCormick, G.C.: Radar observations of the alignment of precipitation particles by electrostatic fields in thunderstorms. *J. Geo. Res.* **81**, 5353–5357 (1976)
- Ho, C.H., Lee, J.Y., Ahn, M.H., Lee, H.S.: A sudden change in summer rainfall characteristics in Korea during the late 1970s. *Int. J. Climatol.* **23**, 117–128 (2003)
- Ho, J., Zhang, G., Bukovic, P., Parsons, D.B., Xu, F., Gao, J., Carlin, J.T., Snyder, J.C.: Improving polarimetric radar-based drop size distribution retrieval and rain estimation using deep neural network. *J. Hydrometeorol.* (2023). <https://doi.org/10.1175/JHM-D-22-0166.1>
- Houze, R.A., Jr.: *Cloud Dynamics*. Academic, San Diego (2014)
- Hubbert, J.C., Ellis, S.M., Chang, W.Y., Rutledge, S., Dixon, M.: Modeling and interpretation of S-band ice crystal depolarization signatures from data obtained by simultaneously transmitting horizontally and vertically polarized fields. *J. Appl. Meteorol. Climatol.* **53**, 1659–1677 (2014)
- Hyun, Y.K., Kar, S.K., Ha, K.-J., Lee, J.H., et al.: Diurnal and spatial variabilities of monsoonal CG lightning and precipitation and their association with the synoptic weather conditions over South Korea. *Theor. Appl. Climatol.* **102**, 43–60 (2010). <https://doi.org/10.1007/s00704-009-0235-5>
- Kar, S.K., Ha, K.-J.: Characteristic differences of rainfall and cloud-to-ground lightning activity over South Korea during the summer monsoon season. *Mon. Wea. Rev.* **131**, 2312–2323 (2003). [https://doi.org/10.1175/1520-0493\(2003\)131/3C2312:CDORAC/3E2.0.CO;2](https://doi.org/10.1175/1520-0493(2003)131/3C2312:CDORAC/3E2.0.CO;2)
- Kim, H.R., Moon, M., Yun, J., Ha, K.J.: Trends and spatio-temporal variability of summer mean and extreme precipitation across South Korea for 1973–2022. *Asia-Pac. J. Atmos. Sci.* **59**, 385–398 (2023)
- Kim, J.-H., Ho, C.-H., Lee, M.-H., Jeong, J.-H., Chen, D.: Large increase in heavy rainfall associated with tropical cyclone landfalls in Korea after the late 1970s. *Geophys. Res. Lett.* **33**, L18706 (2006). <https://doi.org/10.1029/2006GL027430>
- Kumjian, M.R.: Principles and applications of dual-polarization weather radar. Part I: Description of the polarimetric radar variables. *J. Operat. Meteor.* **1**, 226–242 (2013)
- Kumjian, M.R., Khain, A.P., Benmoshe, N., Ilotoviz, E., Ryzhkov, A.V., Phillips, V.T.J.: The anatomy and physics of ZDR Columns: investigating a polarimetric radar signature with a spectral bin microphysical model. *J. Appl. Meteorol. Climatol.* **53**, 1820–1843 (2014). <https://doi.org/10.1175/JAMC-D-13-0354.1>
- Lu, J., Qie, X., Xiao, X., Jiang, R., Mansell, E.R., Fierro, A.O., Liu, D., Chen, Z., Yuan, S., Sun, M., Yu, H., Zhang, Y., Wang, D., Yair, Y.: Effects of convective mergers on the evolution of microphysical and electrical activity in a severe squall line simulated by WRF coupled with explicit electrification scheme. *J. Geophys. Res. Atmos.* **127**, e2021JD036398 (2022). <https://doi.org/10.1029/2021JD036398>
- MacGorman, D.R., Rust, W.D., Schuur, T.J., Biggerstaff, M.I., Straka, J.M., Ziegler, C.L., Mansell, E.R., Bruning, E.C., Kuhlman, K.M., Lund, N.R., Biermann, N.S., Payne, C., Carey, L.D., Krehbiel, P.R., Rison, W., Eack, K.B., Beasley, W.H.: TELEX the thunderstorm electrification and lightning experiment. *Bull. Am. Meteorol. Soc.* **89**, 997–1014 (2008)
- Mahale, V.N., Zhang, G., Xue, M.: Fuzzy logic classification of S-band polarimetric radar echoes to identify three-body scattering and improve data quality. *J. Appl. Meteorol. Climatol.* **53**, 2017–2033 (2014)
- Mareev, E.A., Dementyeva, S.O.: The role of turbulence in thunderstorm, snowstorm, and dust storm electrification. *J. Geophys. Res. Atmos.* **122**, 6976–6988 (2017)
- Mattos, E.V., Machado, L.A., Williams, E.R., Albrecht, R.I.: Polarimetric radar characteristics of storms with and without lightning activity. *J. Geophys. Res. Atmos.* **121**, 14–201 (2016)
- Mattos, E.V., Machado, L.A., Williams, E.R., Goodman, S.J., Blakeslee, R.J., Bailey, J.C.: Electrification life cycle of incipient thunderstorms. *J. Geophys. Res. Atmos.* **122**, 4670–4697 (2017)
- Merz, R., Blöschl, G.: A process typology of regional floods. *Water Resour. Res.* **39** (2003). <https://doi.org/10.1029/2002WR001952>
- Nielsen, J.K., Maus, C., Rzesanke, D., Leisner, T.: Charge induced stability of water droplets in subsaturated environment. *Atmos. Chem. and Phys.* **11**, 2031–2037 (2011)
- Park, H.S., Ryzhkov, A.V., Zrnić, D.S., Kim, K.E.: The hydrometeor classification algorithm for the polarimetric WSR-88D: Description and application to an MCS. *Weather Forecast.* **24**, 730–748 (2009)

- Price, C., Rind, D.: A simple lightning parameterization for calculating global lightning distributions. *J. Geophys. Res. Atmos.* **97**, 9919–9933 (1992)
- Renni, E., Krausmann, E., Cozzani, V.: Industrial accidents triggered by lightning. *J. Hazard. Mater.* **184**, 42–48 (2010)
- Rutledge, S.A., MacGorman, D.R.: Cloud-to-ground lightning activity in the 10–11 June 1985 mesoscale convective system observed during the Oklahoma-Kansas PRE-STORM project. *Mon. Weather Rev.* **116**, 1393–1408 (1988)
- Ryzhkov, A.V., Zrnić, D.S.: Depolarization in ice crystals and its effect on radar polarimetric measurements. *J. Atmos. Ocean. Technol.* **24**, 1256–1267 (2007)
- Saunders, C.: Charge separation mechanisms in clouds. *Space Sci. Rev.* **137**, 335–353 (2008)
- Schultz, C.J., Carey, L.D., Schultz, E.V., Blakeslee, R.J.: Insight into the kinematic and microphysical processes that control lightning jumps. *Weather Forecast.* **30**, 1591–1621 (2015)
- Schultz, C.J., Carey, L.D., Schultz, E.V., Blakeslee, R.J.: Kinematic and microphysical significance of lightning jumps versus nonjump increases in total flash rate. *Weather Forecast.* **32**, 275–288 (2017)
- Shapiro, M.A.: Frontogenesis and geostrophically forced secondary circulation in the vicinity of jet stream-frontal zone system. *J. Atmos. Sci.* **38**, 954–973 (1981)
- Shrestha, Y., Zhang, Y., Doviak, R., Chan, P.W.: Lightning flash rate nowcasting based on polarimetric radar data and machine learning. *Int. J. Remote Sens.* **42**, 6762–6780 (2021)
- Solomon, R., Baker, M.: Lightning flash rate and type in convective storms. *J. Geophys. Res. Atmos.* **103**, 14041–14057 (1998)
- Stough, S.M., Carey, L.D., Schultz, C.J., Cecil, D.J.: Supercell thunderstorm charge structure variability and influences on spatial lightning flash relationships with the updraft. *Mon. Weather Rev.* **150**, 843–861 (2022)
- Straka, J.M., Zrnić, D.S., Ryzhkov, A.V.: Bulk hydrometeor classification and quantification using polarimetric radar data: Synthesis of relations. *J. Appl. Meteorol. Climatol.* **39**, 1341–1372 (2000)
- Snyder, J.C., Ryzhkov, A.V., Kumjian, M.R., Khain, A.P., Picca, J.C.: A ZDR column detection algorithm to examine convective storm updrafts. *Weather Forecast.* **30**, 1819–1844 (2015)
- Takahashi, T.: Riming electrification as a charge generation mechanism in thunderstorms. *J. Atmos. Sci.* **35**, 1536–1548 (1978)
- Takahashi, T., Kawano, T., Ishihara, M.: Different precipitation mechanisms produce heavy rain with and without lightning in Japan. *J. Meteorol. Soc. Japan.* **93**, 245–263 (2015)
- Thiel, K.C., Calhoun, K.M., Reinhart, A.E., MacGorman, D.R.: GLM and ABI characteristics of severe and convective storms. *J. Geophys. Res. Atmos.* **125** (2020). <https://doi.org/10.1029/2020JD032858>
- Veraverbeke, S., Rogers, B.M., Goulden, M.L., Jandt, R.R., Miller, C.E., Wiggins, E.B., Randerson, J.T.: Lightning as a major driver of recent large fire years in North American boreal forests. *Nat. Clim. Change.* **7**, 529–534 (2017)
- Wang, H., Yuan, S., Liu, Y., Li, Y.: Comparison of the WRF-FDDA-based radar reflectivity and lightning data assimilation for short-term precipitation and lightning forecasts of severe convection. *Remote Sens.* **14**, 5980 (2022). <https://doi.org/10.3390/rs14235980>
- Westra, S., Fowler, H.J., Evans, J.P., Alexander, L.V., Berg, P., Johnson, F., Kendon, E.J., Lenderink, G., Roberts, N.: Future changes to the intensity and frequency of short-duration extreme rainfall. *Rev. Geophys.* **52**, 522–555 (2014)
- Wiens, K.C., Rutledge, S.A., Tessendorf, S.A.: The 29 June 2000 supercell observed during STEPS. Part II: Lightning and charge structure. *J. Atmos. Sci.* **62**, 4151–4177 (2005)
- Zhao, C., Zhang, Y.J., Zheng, D., Zhou, Y., Xiao, H., Zhang, X.: An improved hydrometeor identification method for X-band dual-polarization radar and its application for one summer Hailstorm over Northern China. *Atmos. Res.* **245**, 105075 (2020)
- Zhao, C., Zhang, Y.J., Zheng, D., Liu, X., Zhang, Y., Fan, X., Yao, W., Zhang, W.: Using polarimetric radar observations to characterize first echoes of thunderstorms and nonthunderstorms: A comparative study. *J. Geophys. Res. Atmos.* **127** (2022). <https://doi.org/10.1029/2022JD036671>

**Publisher's Note** Springer Nature remains neutral with regard to jurisdictional claims in published maps and institutional affiliations.

